Optimization and preoperative adjustment design of remote center motion mechanism for minimally invasive surgical robot

Guojun Niu, Bo Pan, Yili Fu[*] and Shuguo Wang

Abstract

In this paper, a new remote center motion (RCM) mechanism called triangle is proposed; this mechanism is simple and with high stiffness. A complete kinematic analysis and optimization algorithm implying AHP which is a combination of quantitative and qualitative analysis method incorporating the requirements for minimally invasive surgery (MIS) are performed to find the optimal link lengths of the manipulator. The results show that for the serial triangle two-link manipulator used to guide the surgical tool, the optimization link angles are 74° and 51°. Prior preoperative adjustment is usually realized by electromagnetic clutch. However, the disadvantage of this method is that the joint is complex, big, and heavy because of gravity balance mechanism. A new preoperative adjustment method realized by resistance compensation is proposed without electromagnetic clutch; the joint is simpler and lighter than the conventional joint.

Keywords: Minimally invasive surgery; Medical robot; Optimization; Remote center motion

Background

Compared with conventional surgery, MIS is accomplished by inserting the surgical tool into the patient's body through small incisions. MIS has some advantages such as less pain, less invasive, less recovery time, fewer postoperative complications. MIS becomes more and more popular and is accepted by the public; many companies and research institutions are engaged in MIS. However, due to small incisions, there are some disadvantages such as lower flexibility of the surgical instruments, easy fatigue, eye-hand incoordination, lack of depth feeling, and reduced view of surgical area. In order to solve the limitation of MIS application, computer and robotics assistance is an appropriate choice.

According to the fixed point constraint, RCM is indispensible in the surgery. There are two main ways to achieve RCM; the first method is a control method which is achieved by kinematic redundancy control, but the high reliability and stability requiremen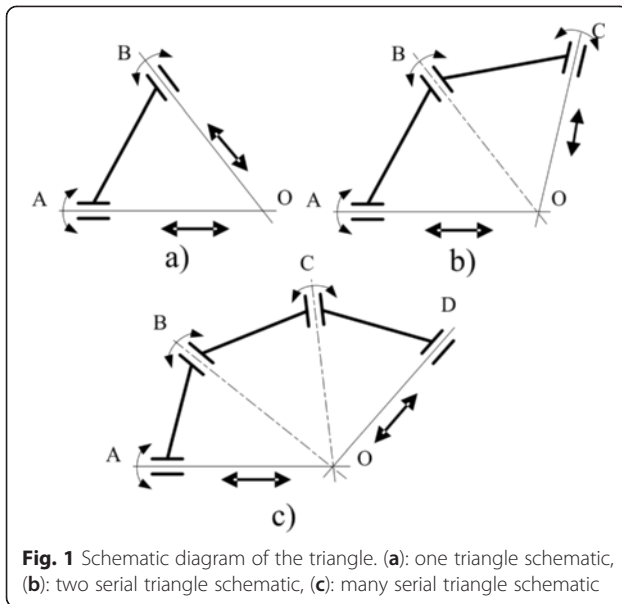t for hardware and algorithms make this method rarely used. There are a small amount of medical robots controlled by this way, such as DLR MIRO surgical robot [1, 2] and TelelapXALF [3] surgical robot. Another method is mechanism constraint, such as parallelogram mechanism, circular mechanism, spherical mechanism, and passive joint.

There are many minimally invasive surgical robots utilizing parallelogram mechanisms to achieve RCM, such as the Black Falcon medical robot developed by MIT [4], the LARS medical robot developed by Johns Hopkins University associated with IBM [5], the RobIn Heart medical robot by the University of Lodz, Poland [6, 7], the DaVinci medical robot introduced by Intuitive Surgical Inc. [8] which received US FDA license, and the Berkeley/UCSF medical robot developed by Cavusoglu M C [9].

The Imperical College London developed the Probot medical robot applying circular mechanism to achieve RCM. The Korea Advanced Institute of Science and Technology developed the KalAR [10] endoscopic surgical robot utilizing circular mechanism to achieve RCM,

* Correspondence: ylfms@hit.edu.cn
State Key Laboratory of Robotics and System, Harbin Institute of Technology, Xidazhi Street, Harbin 150080, China

Niu *et al. Robotics and Biomimetics* (2015) 2:2

Page 2 of 14

Fig. 1 Schematic diagram of the triangle. (**a**): one triangle schematic, (**b**): two serial triangle schematic, (**c**): many serial triangle schematic

Table 1 D-H parameters of the triangle

i	$a_{i-1}/°$	a_i/mm	d_i/mm	$\theta_i/°$
1	$-(\beta_0 + 90)$	0	0	θ_1
2	a_1	0	0	θ_2
3	a_2	0	0	d

too. Freehand Inc. launched the medical robot called Freehand endoscopic achieving RCM by virtue of circular mechanism.

Many institutes and companies have some research achievements utilizing spherical mechanism to achieve RCM, such as the EndoBot robot system [11, 12], LER endoscopic [13], raven medical robot [14], MC²E surgical robot [15], five freedom CURES medical robot [16], laparoscopic holder assisting robot [17], a spherical wrist mechanism robot that replaced human assistant developed by Jeff K. Hsu [18].
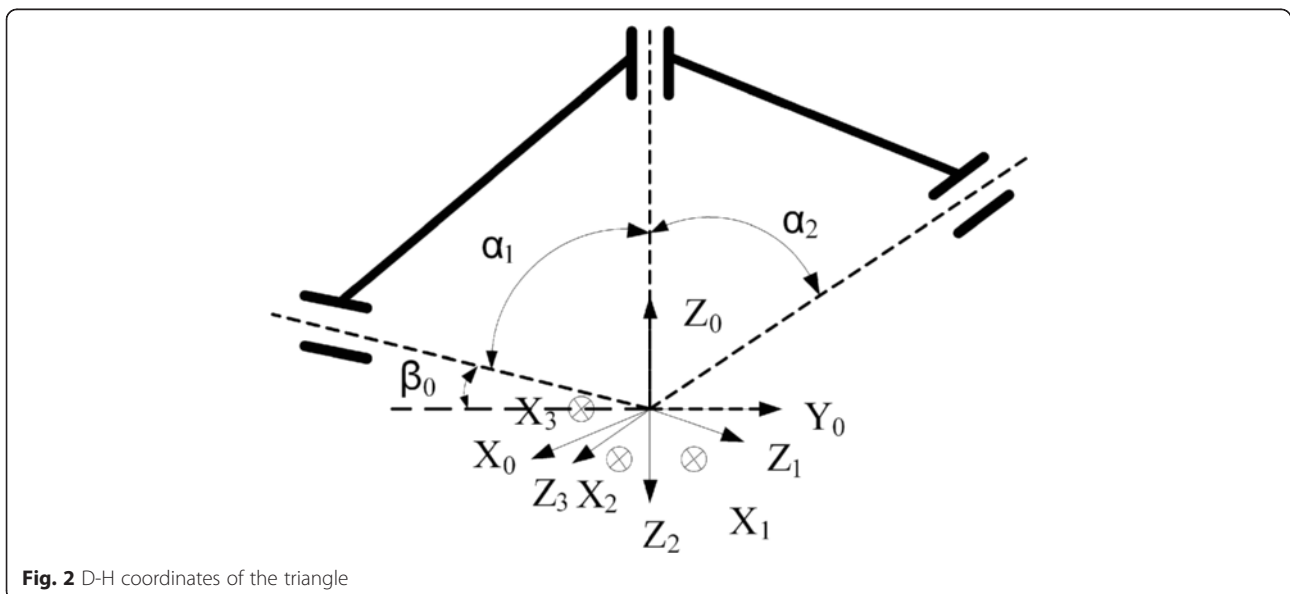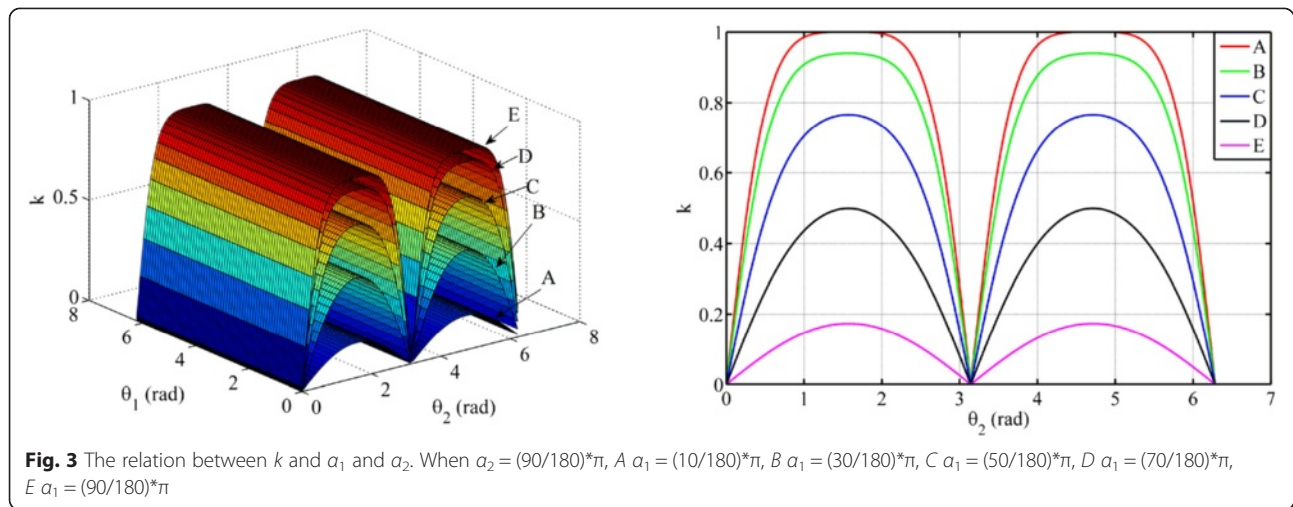
Many medical robots utilize passive joint to achieve RCM, such as AESOP [19] and ZEUS [20] which were developed by Computer Motion and received US Food and Drug Administrator (FDA) license, respectively, and the HISAR medical robot [21] developed by IBM and Johns Hopkins University.

However, there are many institutes and researchers who apply mechanism constraint to achieve RCM, due to the safety and control reliability of mechanism constraint. So the mechanism constraint is the main trend realizing RCM.

Prior preoperative adjustment is important and indispensable for MIS. In order to be easy to adjust the manipulator, electromagnetic clutch is installed between the reducer and the end effector. At the same time, the corresponding gravity compensation mechanism is needed for safety. When power is off, the electromagnetic clutch opens and the end effector can be adjusted easily. After adjustment, turn on the power and the end effector is fixed. However, this method has some shortcomings, such as: the electromagnetic clutch and compensation mechanism will increase the difficulty of joint design and the value and mass of the joint. In the surgery, there are some safety problems because the electromagnetic

Fig. 2 D-H coordinates of the triangle

Niu *et al. Robotics and Biomimetics* (2015) 2:2

Page 3 of 14

Fig. 3 The relation between k and a_1 and a_2. When $a_2 = (90/180)*\pi$, A $a_1 = (10/180)*\pi$, B $a_1 = (30/180)*\pi$, C $a_1 = (50/180)*\pi$, D $a_1 = (70/180)*\pi$, E $a_1 = (90/180)*\pi$

clutch opens when the power is off. The new prior operative adjustment is necessary.

The content of this paper is organized as follows. In the 'Methods' section, the principle and optimization of the mechanism are explained in the kinematic modeling of mechanism. The 'Preoperative adjustment design' section discusses resistance compensation method used in the preoperative adjustment design. The 'Results and discussion' section validates the optimization results and resistance compensation method. Conclusions are drawn in the last section.
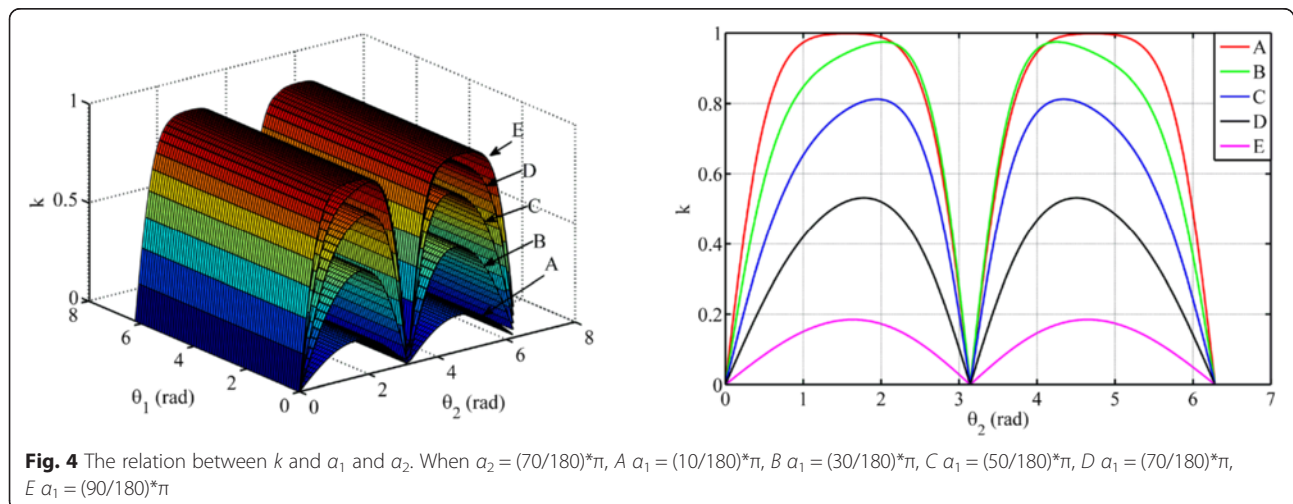
Methods

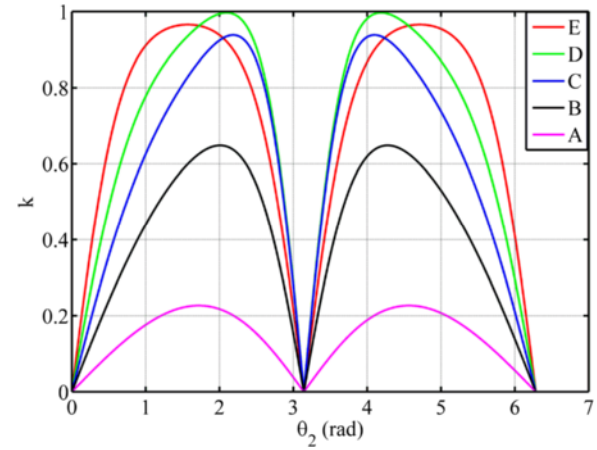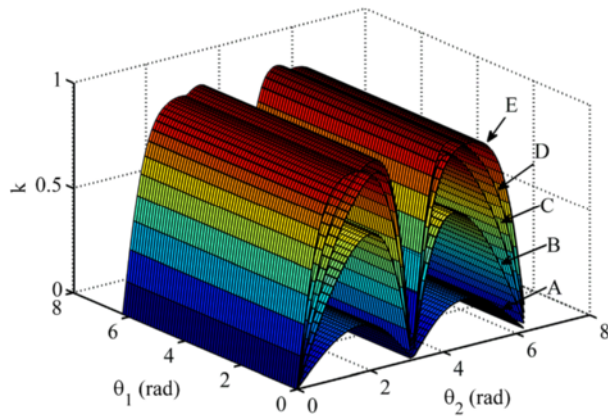### The principle of the triangle mechanism

When rotating or translating along random both sides of the triangle, the trajectory of the motion intersects at a point, which is the fixed point as shown in Fig. 1a. However, many triangles are in series and have common intersection, when rotating along dotted and solid line or translating along the solid line (show in Fig. 1c), the trajectory of the motion intersects at a point which is the fixed point (shown in Fig. 1b). There are only two freedoms which are pitch and roll to achieve RCM in MIS; the ultimate schematic diagram is shown in Fig. 1b.

The kinematic analysis of the triangle mechanism

Kinematic analysis is the foundation of analysis and dynamic modeling of mechanism. D-H coordinates of the triangle are shown in Fig. 2. D-H parameters of the triangle are shown in Table 1.

Fig. 4 The relation between k and a_1 and a_2. When $a_2 = (70/180)*\pi$, A $a_1 = (10/180)*\pi$, B $a_1 = (30/180)*\pi$, C $a_1 = (50/180)*\pi$, D $a_1 = (70/180)*\pi$, E $a_1 = (90/180)*\pi$

Niu *et al. Robotics and Biomimetics* (2015) 2:2

Page 4 of 14

Fig. 5 The relation between k and a_1 and a_2. When $a_2 = (50/180)*\pi$, A $a_1 = (10/180)*\pi$, B $a_1 = (30/180)*\pi$, C $a_1 = (50/180)*\pi$, D $a_1 = (70/180)*\pi$, E $a_1 = (90/180)*\pi$

The forward kinematic is calculated as follows:

$$
{}_3^0T = \begin{pmatrix} n_x & o_x & a_x & p_x \\ n_y & o_y & a_y & p_y \\ n_z & o_z & a_z & p_z \\ 0 & 0 & 0 & 1 \end{pmatrix} \tag{1}
$$

$$
\begin{aligned}
p_x &= ds\alpha_2(c\theta_1 s\theta_2 + c\alpha_2 c\alpha_1 s\theta_1) + dc\alpha_2 s\theta_1 s\alpha_1 \\
p_y &= dc\alpha_2(c\beta_0 c\alpha_1 + c\theta_1 s\beta_0 s\alpha_1) \\
&\quad - ds\alpha_2(c\theta_2 c\beta_0 s\alpha_1 + s\theta_1 s\theta_2 s\beta_0 - c\theta_1 c\theta_2 c\alpha_1 s\beta_0) \\
p_z &= ds\alpha_2(c\theta_2 s\beta_0 s\alpha_1 - c\beta_0 s\theta_1 s\theta_2 + c\theta_1 c\theta_2 c\beta_0 c\alpha_1) \\
&\quad - dc\alpha_2(c\alpha_1 s\beta_0 - c\theta_1 c\beta_0 s\alpha_1)
\end{aligned} \tag{2}
$$
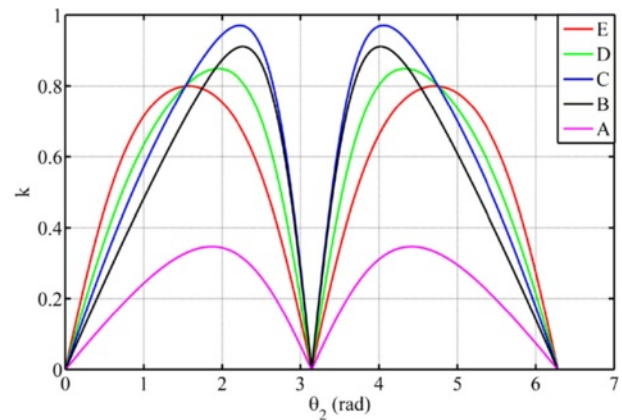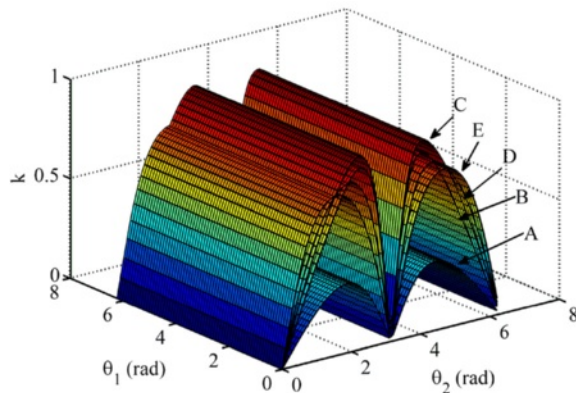
where $c\theta_1 = \cos\theta_1$, $s\theta_1 = \sin\theta_1$, $c\theta_2 = \cos\theta_2$, $s\theta_2 = \sin\theta_2$,

$c\beta_0 = \cos\beta_0$, $s\beta_0 = \sin\beta_0$, $c\alpha_1 = \cos\alpha_1$, $s\alpha_1 = \sin\alpha_1$, $c\alpha_2 = \cos\alpha_2$, $s\alpha_2 = \sin\alpha_2$.

In the surgery, the information about location of the end effector is given by the master, then the inverse kinematic about the corresponding angle θ_i ($i = 1,2$) and expansion length d is obtained as follows:
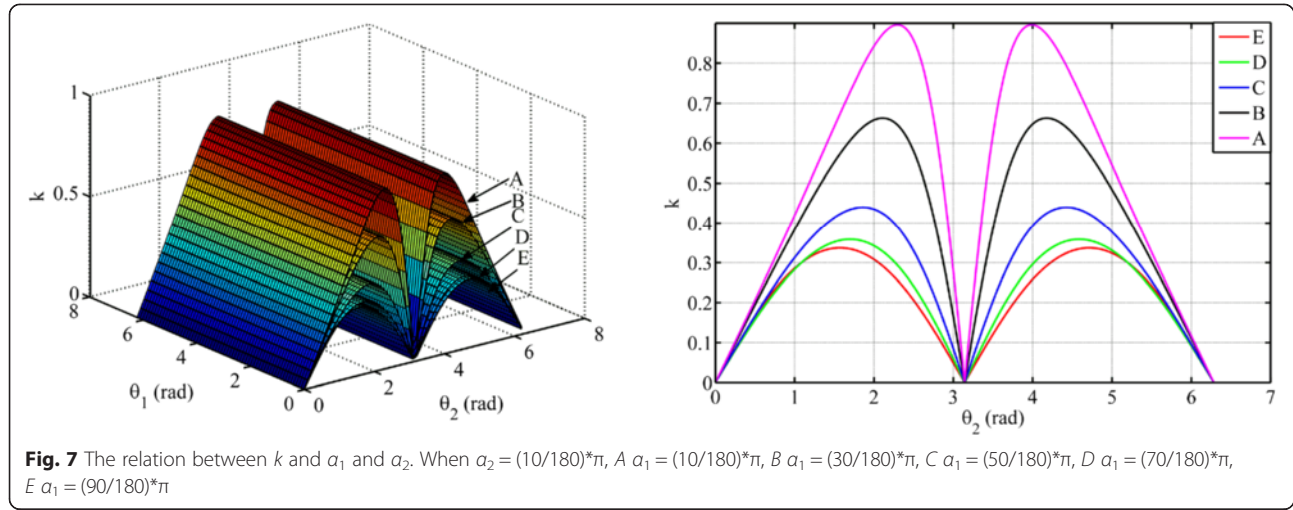
$$
d = \sqrt{(p_x)^2 + \left(p_y\right)^2 + (p_z)^2} \tag{3}
$$

$$
\theta_2 = \pm \arccos\left(\frac{\left(p_y s\alpha_0 - p_z c\alpha_0 + dc\alpha_1 c\alpha_2\right)}{(ds\alpha_1 s\alpha_2)}\right) \tag{4}
$$

Fig. 6 The relation between k and a_1 and a_2. When $a_2 = (30/180)*\pi$, A $a_1 = (10/180)*\pi$, B $a_1 = (30/180)*\pi$, C $a_1 = (50/180)*\pi$, D $a_1 = (70/180)*\pi$, E $a_1 = (90/180)*\pi$

Fig. 7 The relation between k and a_1 and a_2. When $a_2 = (10/180)*\pi$, A $a_1 = (10/180)*\pi$, B $a_1 = (30/180)*\pi$, C $a_1 = (50/180)*\pi$, D $a_1 = (70/180)*\pi$, E $a_1 = (90/180)*\pi$

$$\theta_1 = a \cot \frac{k_1}{k_2} \quad \text{or} \quad \theta_1 = pi + a \cot \frac{k_1}{k_2}$$
$$k_1 = p_x s\alpha_2 s_2 - \left(p_y c\alpha_0 + p_z s\alpha_0 \right) \left(c\alpha_1 s\alpha_2 c_2 + s\alpha_1 c\alpha_2 \right)$$
$$k_2 = p_x (c\alpha_1 s\alpha_2 c_2 + s\alpha_1 c\alpha_2) + sc\alpha_1 s\alpha_2 c_2$$
$$+ s\alpha_2 s_2 \left(p_y c\alpha_0 + p_z s\alpha \right)$$

$$(5)$$

Jacobian matrix is deduced by differential transformation method. The Jacobian matrix is as follows:

For rotary joint, the Jacobian matrix is as follows:

$$J_i = \left[(p \times n)_z \quad (p \times o)_z \quad (p \times n)_z \quad n_z \quad o_z \quad a_z \right]^T$$

$$(6)$$

For translational joint, the Jacobian matrix is as follows:

$$J_i = \left[n_z \quad o_z \quad a_z \quad 0 \quad 0 \quad 0 \right] dq_j$$

$$(7)$$

n, o, a is the rotational transformation matrix vector from the ith link to the end coordinate system of the robot, and p is the position vector from the ith link to the end coordinate system of robot.

The pose of the RCM is mainly considered, as $d = 0$. The Jacobian of remote center mechanism is as follows:

$$J_3 = \left[0 \ 0 \ 1 \ 0 \ 0 \ 0 \right]^T$$

$$(8)$$

$$J_2 = \left[0 \ 0 \ 0 \ 0 \ \sin\alpha_2 \ \cos\alpha_2 \right]^T$$

$$(9)$$

$$J_1 = \begin{bmatrix} 0 & 0 & 0 & \sin\theta_2 \sin\alpha_1 \\ \cos\alpha_1 \sin\alpha_2 + \cos\theta_2 \sin\alpha_1 \cos\alpha_2 \\ \cos\alpha_1 \cos\alpha_2 - \cos\theta_2 \sin\alpha_1 \sin\alpha_2 \end{bmatrix}^T$$

$$(10)$$

$$J = \left[J_1 \quad J_2 \quad J_3 \right]$$

$$(11)$$

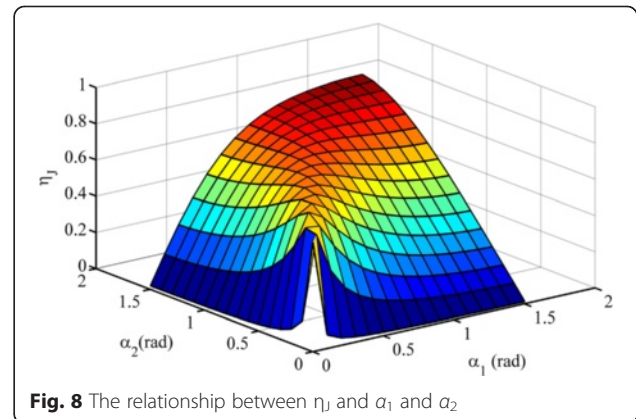However, roll and pitch are the main issue. The simplification of Jacobian matrix is expressed as follows:

$$J = \begin{pmatrix} \sin\alpha_1 \sin\theta_2 & 0 \\ \cos\theta_2 \sin\alpha_1 \cos\alpha_2 + \cos\alpha_1 \sin\alpha_2 & \sin\alpha_2 \end{pmatrix}$$
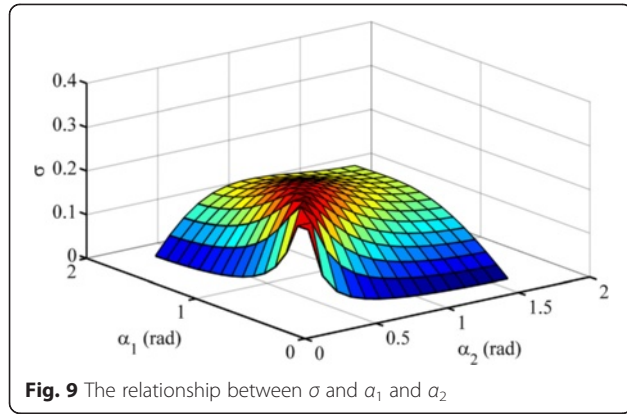
$$(12)$$

Performance analysis of the triangle mechanism

The Jacobi condition number is expressed as:

$$k' = \begin{cases} \|J(q)\| \|J^{-1}(q)\| & m = n \\ \|J(q)\| \|J^+(q)\| & m < n \end{cases}$$

$$(13)$$

where $\|J(q)\| = \sqrt{tr\left(J(q) \omega J(q)^T \right)}$, $\omega = 1/n$, n is the $J(q)$ matrix number, $J^+(q) = J^T(q)(J(q)J^T(q))^{-1}$. The relation

Fig. 8 The relationship between η_J and a_1 and a_2

Niu *et al. Robotics and Biomimetics* (2015) 2:2

Page 6 of 14

Fig. 9 The relationship between σ and α_1 and α_2

Table 2 Judgment matrix value

	a_1	a_2	a_3	a_4	a_5	a_6	a_7	a_8
a_1	1	1	1	2	2	2	2	2
a_2	1	1	1	2	2	2	2	2
a_3	1	1	1	2	2	2	2	2
a_4	0.5	0.5	0.5	1	1	1	1	1
a_5	0.5	0.5	0.5	1	1	1	1	1
a_6	0.5	0.5	0.5	1	1	1	1	1
a_7	0.5	0.5	0.5	1	1	1	1	1
a_8	0.5	0.5	0.5	1	1	1	1	1

between the condition number with singular value is written as follows:

$$k' = \frac{\mu_l}{\mu_r} \tag{14}$$

So, $1 \le k' \le \infty$ μ_l is maximum singular value, μ_r is minimum singular value.

Dexterity is expressed as the inverse of the Eq. 14, so $0 \le k \le 1$.

$$k = \frac{\mu_r}{\mu_l} \tag{15}$$

Figure 3 indicates the relation between k and α_1 and α_2; the best configuration is $\alpha_1 = (90/180)*\pi$ and $\alpha_2 = (90/180)*\pi$. Figure 4 indicates the relation between k and α_1 and α_2; the best configuration is $\alpha_2 = (70/180)*\pi$ and $\alpha_1 = (90/180)*\pi$. Figure 5 indicates the relation between k and α_1 and α_2; the best configuration is $\alpha_2 = (50/180)*\pi$ and $\alpha_1 = (70/180)*\pi$. Figure 6 indicates the relation between k and α_1 and α_2; the best configuration is $\alpha_2 = (30/180)*\pi$ and $\alpha_1 = (50/180)*\pi$. Figure 7 indicates the relation between k and α_1 and α_2; the best
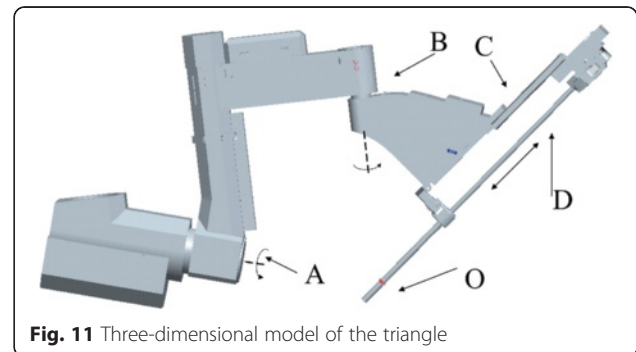
configuration is $\alpha_2 = (10/180)*\pi$ and $\alpha_1 = (10/180)*\pi$. From the above analysis, k is related with posture of mechanism.
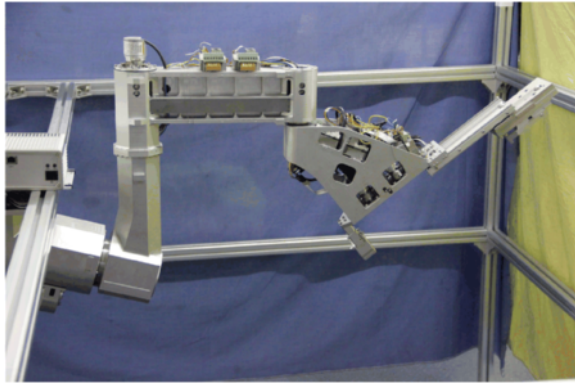
Gosselin [22] defined global performance indicator (GPI) as follows:

$$\eta_J = \frac{\int_\omega k d\varpi}{\int d\varpi} \tag{16}$$

where ϖ is the reachable workspace and k is the dexterity of mechanism. The relationship between η_J and α_1 and α_2 is shown in Fig. 8. The best configuration is $(0.5\pi, 0.5\pi)$. GPI is the average level of performance of mechanism in the whole workspace. GPI does not indicate the performance fluctuations margin. Shi et al. [23] define performance fluctuations indicator (PFI) by Eq. 17. PFI is the supplementary of GPI. The relationship between σ and α_1 and α_2 is shown in Fig. 9.

$$\sigma = \sqrt{\frac{\int_\varpi \left(\frac{1}{k - \eta_J}\right)^2 d\varpi}{\int_\varpi d\varpi}} \tag{17}$$

Fig. 10 The relationship between σ_J and α_1 and a_2

Fig. 11 Three-dimensional model of the triangle

Niu *et al. Robotics and Biomimetics* (2015) 2:2

Page 7 of 14

Fig. 12 RCM mechanism prototype

However, in order to explore the potential of mechanism, the improvement of GFI (IGFI) [24] is shown as follows. The relationship between σ_J and α_1 and α_2 is shown in Fig. 10.

$$\sigma_J = \frac{\int_{\varpi} k(k-\eta_J)^2 d\varpi}{\int_{\varpi} d\varpi} \tag{18}$$

Optimization of the triangle mechanism

GPI (a1), GFI (a2), IGF (a3), mechanism mass (a4), mechanism stiffness (a5), workspace surface area (a6), collision probability (a7), and gravity torque (a8) are chosen as evaluation indicators. However, three indexes consisting of a1, a2, and a3 are the main factors, and the others are auxiliary factors. Each factor weight is divided by AHP which is a combination of quantitative and

qualitative analysis method and is proposed by T. L. Saaty. Value standards of judgment matrix is shown in the paper [25]. Judgment matrix value is achieved and shown in Table 2. When CI = 0 and CR = 0, the judgment matrix is completely consistent.

The weights of a1, a2, a3, a4, a5, a6, a7, and a8 are 0.1818, 0.1818, 0.1818, 0.0909, 0.0909, 0.0909, 0.0909, and 0.0909, respectively. CI = CR = 0. Judgment matrix is completely consistent.

The optimization algorithm is nonlinear programming algorithm.

Constraint conditions: $0 < \alpha_1 \le 0.5\pi$, $0 < \alpha_2 \le 0.5\pi$.

Objective function:

$$\begin{aligned} \min f = {}^{a1}\!\big/\!a\max * 0.1818 + {}^{a2}\!\big/\!a2\max \\ * 0.1818 - {}^{a3}\!\big/\!a3\max * 0.1818 - {}^{a4}\!\big/\!a4\max \\ * 0.0909 + {}^{a5}\!\big/\!a5\max * 0.0909 + {}^{a6}\!\big/\!a6\max \\ * 0.0909 - {}^{a7}\!\big/\!a7\max * 0.0909 - {}^{a8}\!\big/\!a8\max \\ * 0.0909 \end{aligned} \tag{19}$$

Optimization result of α_1 and α_2 is 74.1955° and 51.4°, respectively; after rounding, $\alpha_1 = 74°$ and $\alpha_2 = 51°$.

Three-dimensional model is shown in Fig. 11. The principle prototype is shown in Fig. 12.

**Preoperative adjustment design**

Preoperative adjustment is an important part for surgical operation. In order to adjust the surgical instrument and manipulator conveniently, many researchers try to design some back-drivable equipments; however, due to the safety of medical equipments, these devices are rarely used. In order to accomplish preoperative adjustment, electromagnetic clutches are used in the medical devices. However,
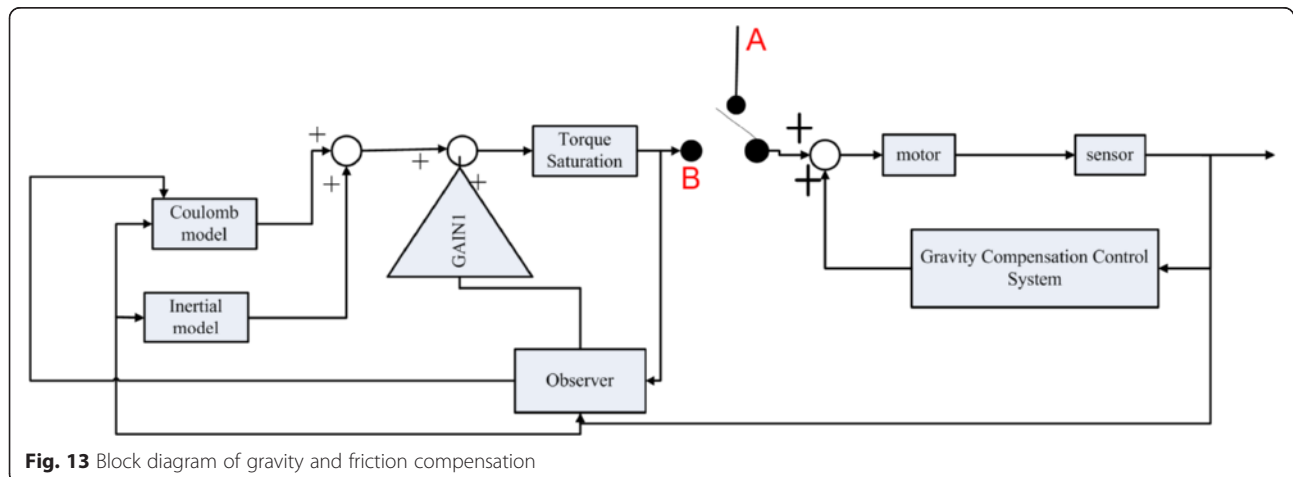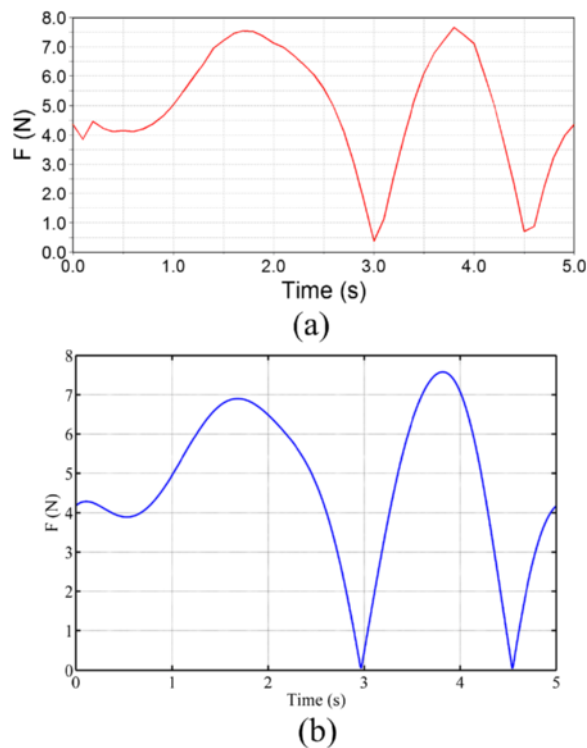

Fig. 13 Block diagram of gravity and friction compensation

Niu *et al. Robotics and Biomimetics* (2015) 2:2

Page 8 of 14
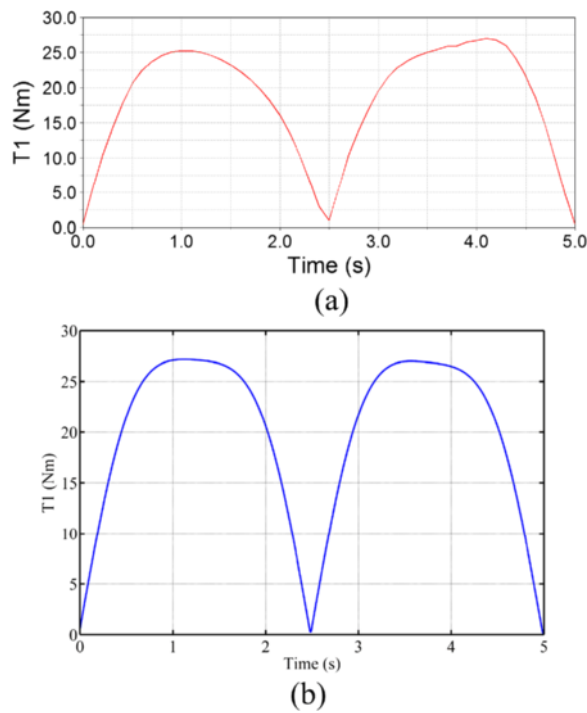
Fig. 14 Joint 1 torque diagram. (**a**): adams simulation result, (**b**): Matlab simulation result
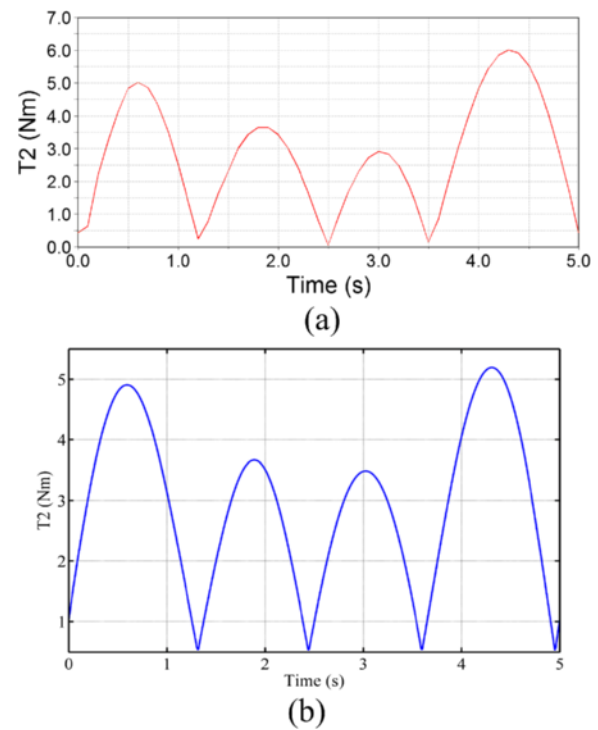
Fig. 16 Joint 3 force diagram (**a**): adams simulation result, (**b**): Matlab simulation result
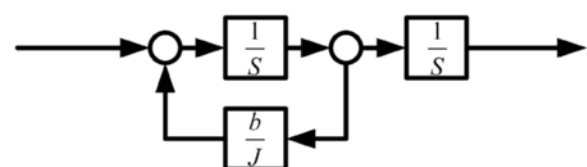

Fig. 15 Joint 2 torque diagram (**a**): adams simulation result, (**b**): Matlab simulation result

clutches increase the weight and volume of the device which leads to vibration and unstable equipment. So an easy way to achieve preoperative adjustment is needed.
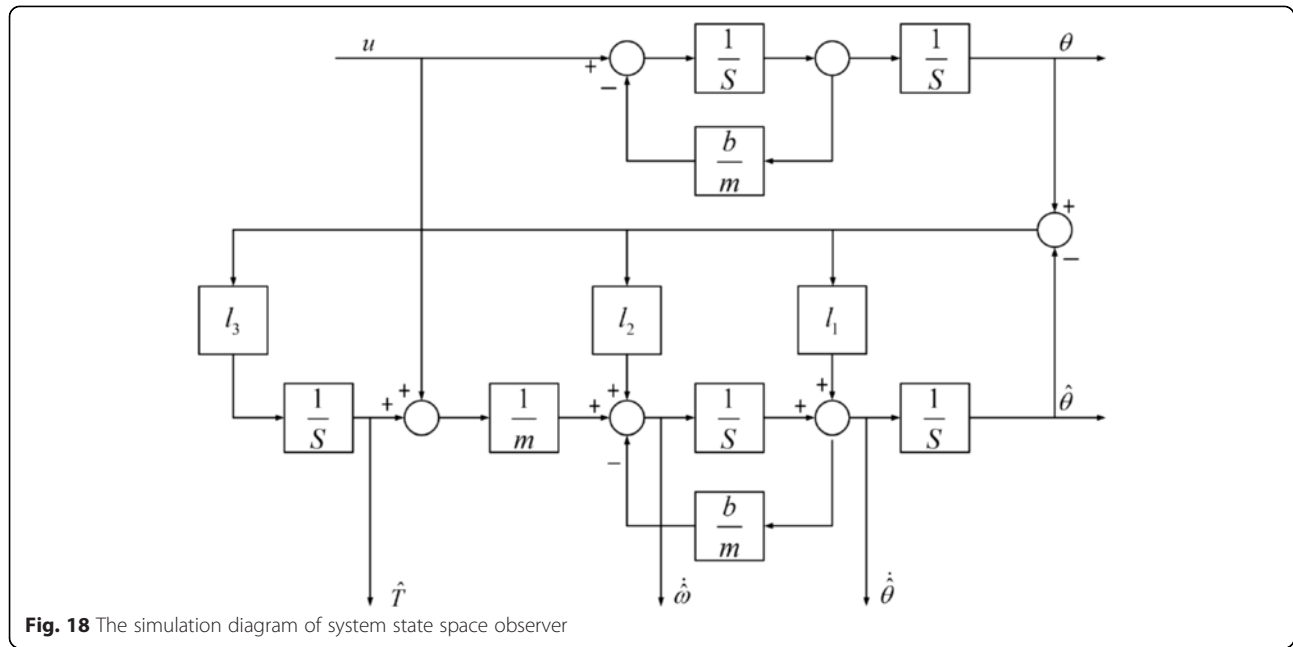
When surgeons try to move the manipulators to the appropriate location, gravity torque and friction torque are the main obstacles to overcome; however, the prior way which used electromagnetic clutches is not conventional because surgeons have to overcome resistance that is mentioned previously. A new way to adjustment is realized by gravity and friction compensation. When the surgeon wants to adjust the manipulator poster or location, a button is pressed and then the control system works. The surgeon moves the manipulator easily, and after adjustment, the button is released and the manipulator keeps stable. The control block diagram is shown in Fig. 13.

The kinetic energy and gravitational potential energy of the first link are calculated in Eq. 20.

Fig. 17 The joint model

Niu *et al. Robotics and Biomimetics* (2015) 2:2

Page 9 of 14

Fig. 18 The simulation diagram of system state space observer

$$dK_1 = \frac{1}{2}(^0v_1)dm = \frac{1}{2}(Q_1^0)(^0T_1)(^ir_1)(^ir_1)^T(^0T_1)^T(Q_1^0)^T(\dot{\theta}_1)^2 dm$$

$$K_1 = \int dK_1 = \frac{1}{2}(Q_1^0)(^0T_1)\int(^ir_1)(^ir_1)^T dm(^0T_1)^T(Q_1^0)^T(\dot{\theta}_1)^2$$

$$= \frac{1}{2}(Q_1^0)(^0T_1)I_1(^0T_1)^T(Q_1^0)^T(\dot{\theta}_1)^2$$

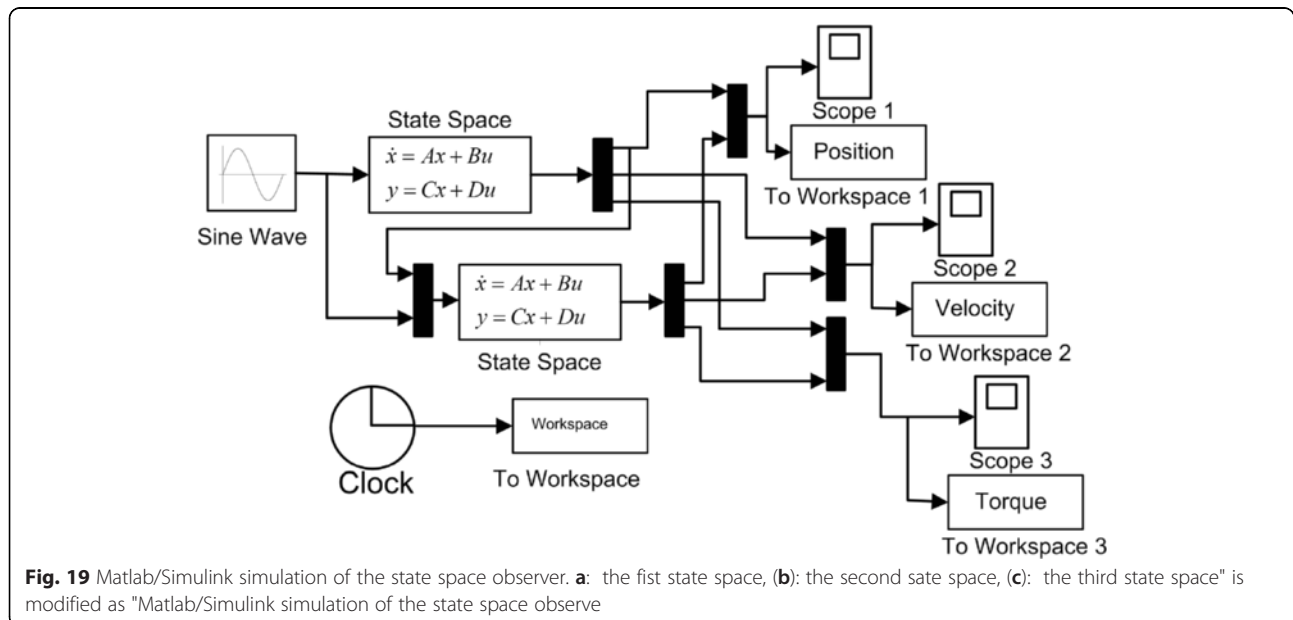$$P_1 = -m_1g(^0T_1{}^i\overline{r_1})$$

(20)

The kinetic energy and gravitational potential energy of the second link are calculated in Eq. 21.

$$K_2 = \int dK_2 = \frac{1}{2}\left((Q_1^0)(^0T_2)\int(^ir_2)(^ir_2)^T dm(^0T_2)^T(Q_1^0)^T\right.$$

$$\times(\dot{\theta}_1)^2 + 2Q_1^0(^0T_2)\int(^ir_2)(^ir_2)^T dm(^0T_2)^T(Q_2^0)^T\dot{\theta}_1\dot{\theta}_2$$

$$+Q_2^{00}T_2\int(^ir_2)(^ir_2)^T dm(^0T_2)^T(Q_2^0)^T(\dot{\theta}_2)^2) = \frac{1}{2}$$

$$\times\left((Q_1^0)(^0T_2)I_2(^0T_2)^T(Q_1^0)^T(\dot{\theta}_1)^2 + 2Q_1^0(^0T_2)I_2\right.$$

$$\times(^0T_2)^T(Q_2^0)^T\dot{\theta}_1\dot{\theta}_2 + Q_2^{00}T_2I_2(^0T_2)^T(Q_2^0)^T(\dot{\theta}_2)^2)$$

$$P_2 = -m_2g(^0T_2{}^i\overline{r_2})$$

(21)

Fig. 19 Matlab/Simulink simulation of the state space observer. **a**: the fist state space, (**b**): the second sate space, (**c**): the third state space" is modified as "Matlab/Simulink simulation of the state space observe

Niu *et al. Robotics and Biomimetics* (2015) 2:2

Page 10 of 14

The kinetic energy and gravitational potential energy of the third link are calculated in Eq. 22.

$$
\begin{aligned}
K_3 = \frac{1}{2} & \left((Q_1^0)(^0T_3) \int dm(^ir_3)(^ir_3)^T(^0T_3)^T(Q_1^0)^T \right. \\
& \times \left(\dot{\theta}_1\right)^2 + 2Q_1^0(^0T_3)\int dm(^ir_2)(^ir_2)^T(^0T_3)^T \\
& \times (Q_2^0)^T\dot{\theta}_1\dot{\theta}_2 + 2Q_1^{00}T_3\int (^ir_3)(^ir_3)^T dm(^0T_3)^T \\
& \times (Q_3^0)^T\dot{\theta}_1\dot{\theta}_3 + 2Q_2^{00}T_3\int (^ir_3)(^ir_3)^T dm(^0T_3)^T \\
& \times (Q_3^0)^T\dot{\theta}_2\dot{\theta}_3 + Q_2^{00}T_3\int (^ir_3)(^ir_3)^T dm(^0T_3)^T \\
& \times (Q_2^0)^T\left(\dot{\theta}_2\right)^2 + Q_3^{00}T_3\int (^ir_3)(^ir_3)dm^T(^0T_3)^T \\
& \times (Q_3^0)^T\left(\dot{\theta}_3\right)^2 \right) = \frac{1}{2}\left((Q_1^0)(^0T_3)I_3(^0T_3)^T(Q_1^0)^T \right. \\
& \times \left(\dot{\theta}_1\right)^2 + 2Q_1^0(^0T_3)I_3(^0T_3)^T(Q_2^0)^T\dot{\theta}_1\dot{\theta}_2 \\
& + 2Q_1^{00}T_3I_3(^0T_3)^T(Q_3^0)^T\dot{\theta}_1\dot{\theta}_3 + 2Q_2^{00}T_3I_3(^0T_3)^T \\
& \times (Q_3^0)^T\dot{\theta}_2\dot{\theta}_3 + Q_2^{00}T_3I_3(^0T_3)^T(Q_2^0)^T\left(\dot{\theta}_2\right)^2 \\
& \left. + Q_3^{00}T_3I_3\left(^0T_3\right)^T(Q_3^0)^T\left(\dot{\theta}_3\right)^2 \right) \quad P_3 = -m_3g\left(^0T_2{}^i\overline{r_3}\right)
\end{aligned}
$$

$$(22)$$

Lagrange equation is show shown in Eq. 23.

$$
\begin{aligned}
& K = K_1 + K_2 + K_3 \\
& P = P_1 + P_2 + P_3 \\
& L = K - P \\
& T_i = \frac{d}{dt}\left[\frac{\partial L}{\partial \dot{q}_i}\right] - \frac{\partial L}{\partial q_i}
\end{aligned}
$$

$$(23)$$

The three-dimensional model is simulated by dynamic analysis software ADAMS, and the rotary joint information can be measured. The simulation condition is shown in Eq. 24. By comparison of two figures, the difference between the two pictures of Figs. 14, 15, and 16 is very small, and dynamic model of RCM mechanism is right.
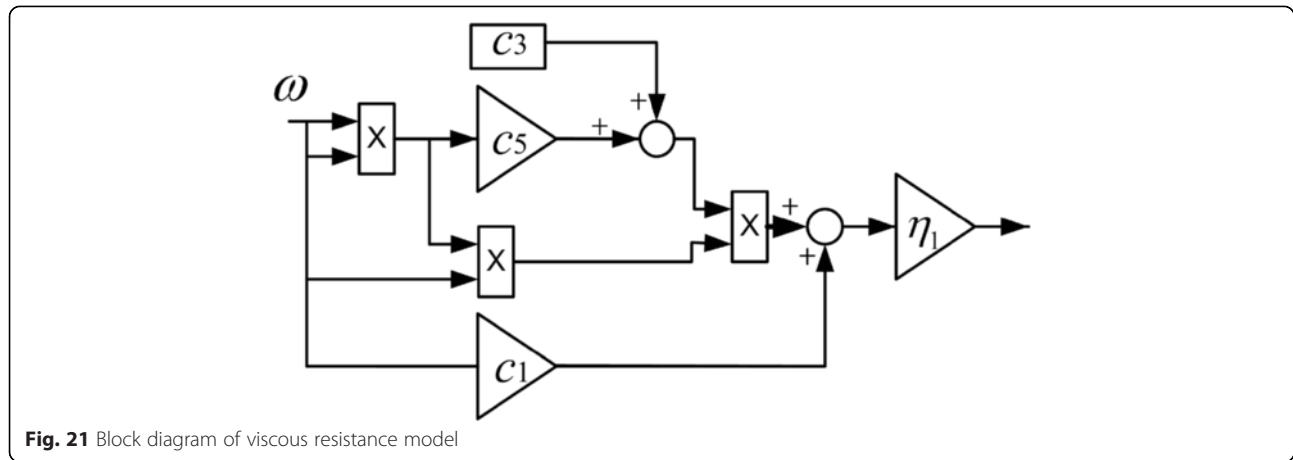
$$
\begin{aligned}
& \theta_1 = 0.5 * \text{pi} * \sin((2 * \text{pi}/5) * t); \\
& \theta_2 = -1.4 * \sin((2 * \text{pi}/5) * t - 0.5 * \text{pi}) - 1.4; \\
& d = 0.075 * \sin((0.4 * \text{pi}) * t - 0.5 * \text{pi}) + 0.075;
\end{aligned}
$$

$$(24)$$

The transfer function between the joint positions and joint motor torque is Eq. 25. The joint model is shown in Fig. 17. The state space equation is achieved by Eq. 26. The state space equation in matrix form is Eq. 27.

$$
G(s) = \frac{1}{Js + b} \cdot \frac{1}{s}
$$

$$(25)$$
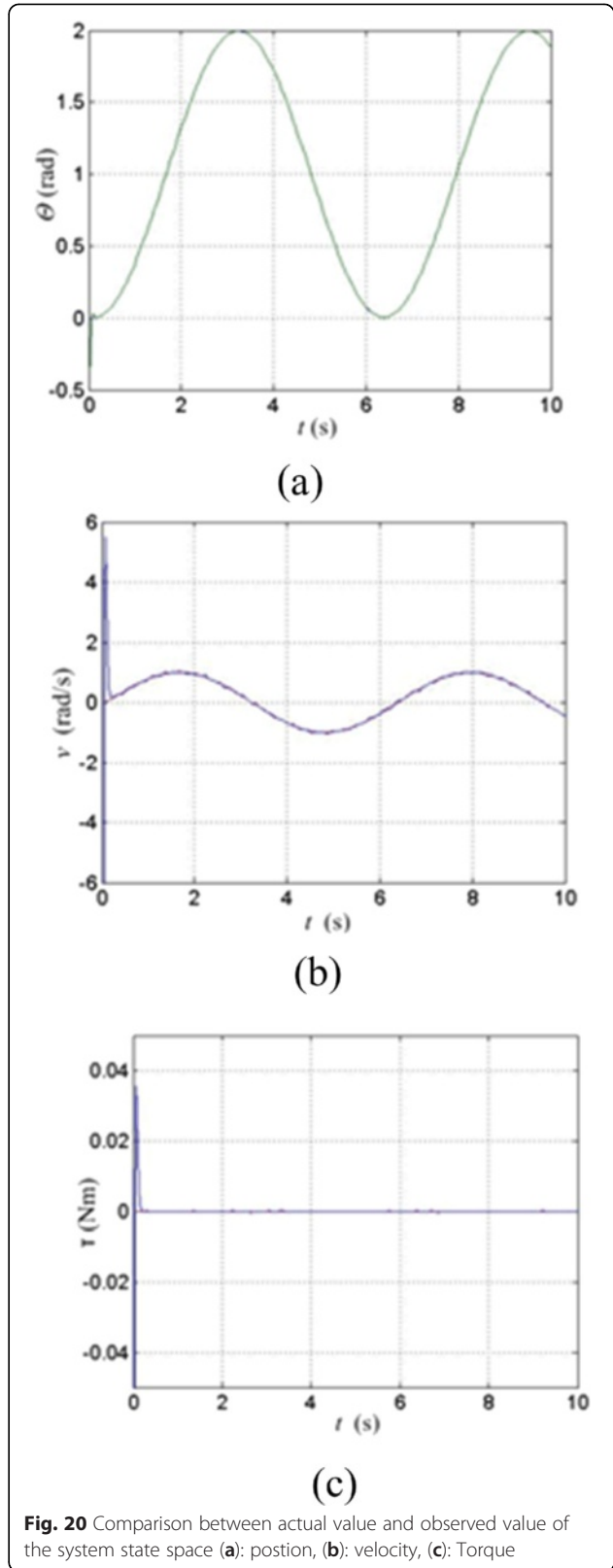
Fig. 20 Comparison between actual value and observed value of the system state space (**a**): postion, (**b**): velocity, (**c**): Torque

Niu *et al. Robotics and Biomimetics* (2015) 2:2

Page 11 of 14

Fig. 21 Block diagram of viscous resistance model

$$\begin{cases} \dot{x}(t) = Ax(t) + Bu(t) \\ \quad y(t) = Cx(t) \end{cases}$$

$$(26)$$

where $A = \begin{bmatrix} 0 & 1 & 0 \\ 0 & -\dfrac{b}{J} & \dfrac{1}{J} \\ 0 & 0 & 0 \end{bmatrix} = \begin{bmatrix} 0 & 1 & 0 \\ 0 & -10 & 100000 \\ 0 & 0 & 0 \end{bmatrix}$ $B =$

$\begin{bmatrix} 0 \\ \dfrac{1}{J} \\ 0 \end{bmatrix} = \begin{bmatrix} 0 \\ 100000 \\ 0 \end{bmatrix}$ $C = \begin{bmatrix} 1 & 0 & 0 \end{bmatrix}$

$$\begin{cases} \begin{bmatrix} \dot{\theta} \\ \dot{\omega} \\ \dot{T}_d \end{bmatrix} = \begin{bmatrix} 0 & 1 & 0 \\ 0 & -\dfrac{b}{J} & -\dfrac{1}{J} \\ 0 & 0 & 0 \end{bmatrix} \begin{bmatrix} \theta \\ \omega \\ T_d \end{bmatrix} + \begin{bmatrix} 0 \\ \dfrac{u}{m} \\ 0 \end{bmatrix} \\ \quad \theta = \begin{bmatrix} 1 & 0 & 0 \end{bmatrix} \begin{bmatrix} \theta \\ \omega \\ T_d \end{bmatrix} \end{cases}$$

$$(27)$$

The observability matrix of the joint system is calculated by Eq. 28 because viscous friction coefficient b and

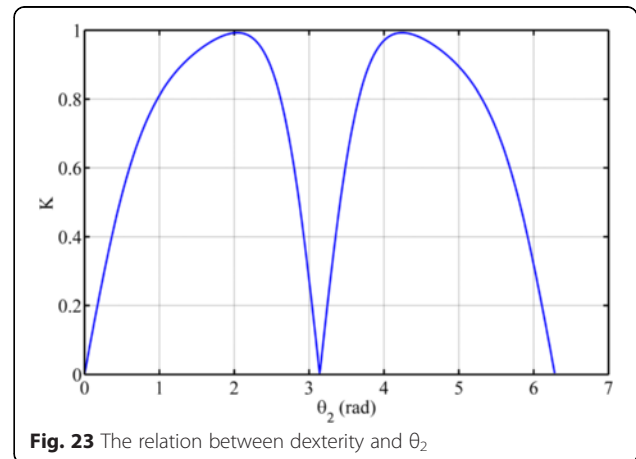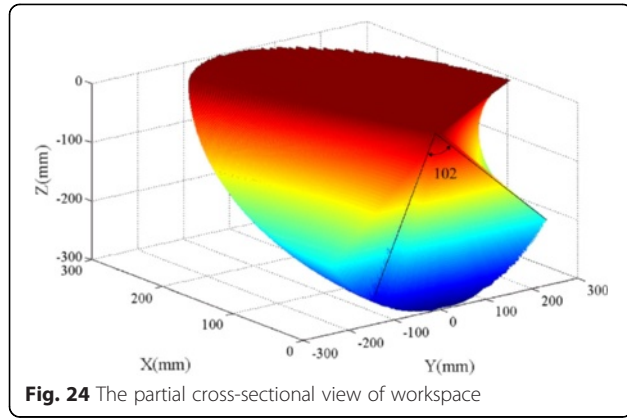**Fig. 22** Block diagram of inertia model
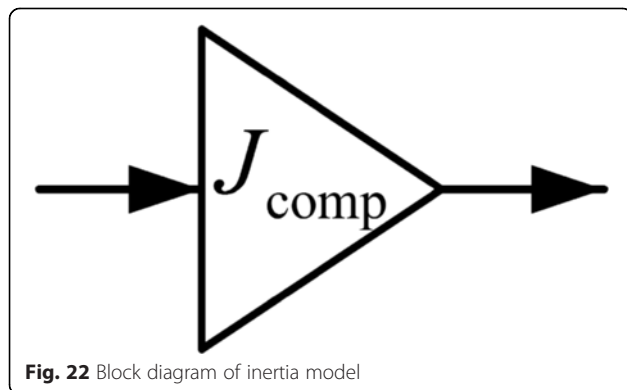
moment of inertia J is not zero. Eq. 29 is achieved, and the system is observable.

$$\begin{bmatrix} C^T & A^T C^T & \dots & (A^T)^2 C^T \end{bmatrix} = \begin{bmatrix} 1 & 0 & 0 \\ 0 & 1 & -b/J \\ 0 & 0 & -1/J \end{bmatrix} \quad (28)$$

$$\text{rank} \begin{bmatrix} C^T & A^T C^T & \dots & (A^T)^{n-1} C^T \end{bmatrix} = 3 \quad (29)$$

The three poles of the system is 0, −10, and 10. According to the principle, the poles of the state observer are $\lambda_1 = -60$, $\lambda_2 = -60 + 10i$, and $\lambda_3 = -60 - 10i$. The characteristic polynomial of the desired observer is deduced by Eq. 30. The polynomial coefficients is $aa_1 = 180$, $aa_2 = 10800$, and $aa_3 = 216100$. The selection matrix is obtained by Eq. 31. Eq. 32 is the general expression of the state observer. The diagram of the state observer is shown in Fig. 18. Matlab/simulink simulation is shown in Fig. 19. Figure 20 is a comparison between actual value and observed value of the system state space. In the beginning, the observer has some vibration; however, the observer follows

Fig. 23 The relation between dexterity and θ_2

Niu *et al. Robotics and Biomimetics* (2015) 2:2

Page 12 of 14

Fig. 24 The partial cross-sectional view of workspace

the original system soon and achieves reliable tracking in the later.

$$(s - \lambda_1)(s - \lambda_2)(s - \lambda_3) = s^3 + 180s^2 + 10800s + 216,100 \tag{30}$$

$$\tilde{L}^T = \begin{bmatrix} e_1 & e_2 & e_3 \end{bmatrix} = \begin{bmatrix} aa_3 - a_3 & aa_2 - a_2 & aa_1 - a_1 \end{bmatrix}$$
$$Q = \begin{bmatrix} C^T & A^T C^T & (A^T)^2 C^T \end{bmatrix} \begin{bmatrix} a_2 & a_1 & 1 \\ a_1 & 1 & 0 \\ 1 & 0 & 0 \end{bmatrix}$$
$$L^T = \tilde{L}^T Q^{-1} = \begin{bmatrix} 170 & 9200 & 2.2 \end{bmatrix} \tag{31}$$

$$\dot{\hat{x}}(t) = (A - L \cdot C_{obs})\hat{x}(t) + Ly(t) + Bu(t) \tag{32}$$

where $C_{obs} = \begin{bmatrix} 1 & 0 & 0 \end{bmatrix}$ and L is the selection matrix. $\hat{x}(t)$ is the state observer value, and $y(t)$ is the actual

value of the joint. $u(t)$ is the theoretical output torque of the joint motor.

Eq. 33 is a viscous resistance model which is established by polynomial form. However, viscous resistance compensation is the fraction of the actual resistance. The actual viscous resistance compensation is finally determined by Eq. 34. The viscous resistance model is shown in Fig. 21. Eq. 35 is an inertial model. However, inertial model compensation is the fraction of the actual inertial resistance, and the actual inertial resistance compensation is finally determined by Eq. 36. Considering that the velocity and acceleration is relatively low, the simplification of inertial resistance is determined by Eq. 37. The inertia model is shown in Fig. 22.

$$T_{viscous} = c_1 \cdot \hat{v} + c_2 \cdot \hat{v}^3 + c_3 \cdot \hat{v}^5 \tag{33}$$

$$T_{comp\_vis} = \eta_1 \cdot T_{viscous} \tag{34}$$

$$T_{inertial} = Ma\,(pos) \times acc + Cor\,(pos, vel) \tag{35}$$

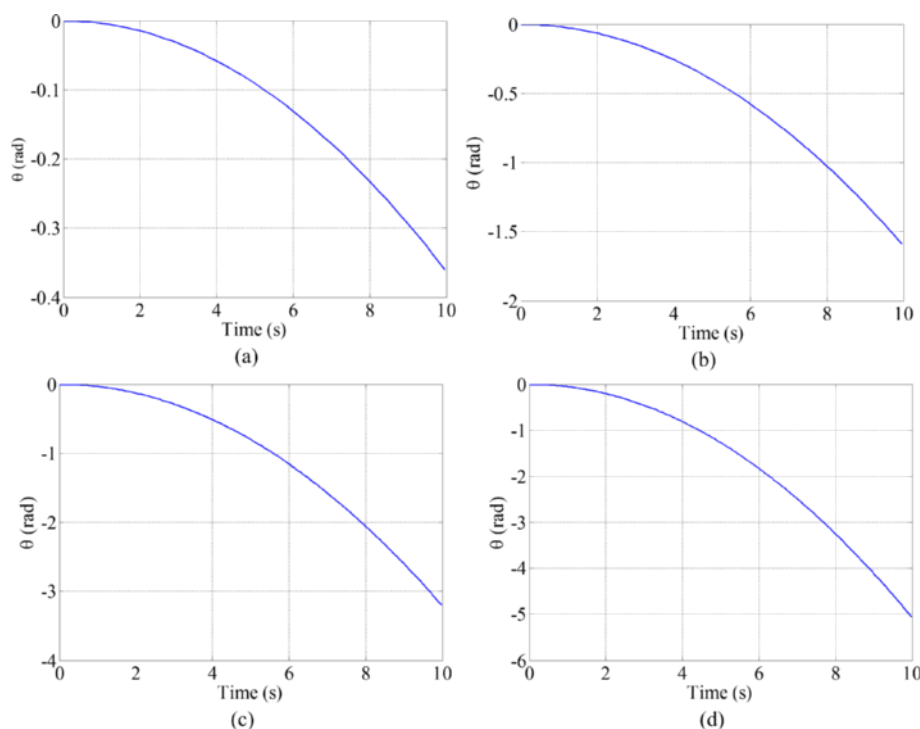Where Ma(pos) is the inertial matrix, acc is the acceleration, and Cor(pos, vel) is the centripetal and coriolis force.

$$T_{comp\_ine} = \eta_2 \cdot T_{inertial} \tag{36}$$

$$J_{comp} = \eta_2 \cdot J \tag{37}$$

Results and discussion

The dexterity of the triangle mechanism is shown in Fig. 23. The paper [26] indicates that surgeons in a MIS

Fig. 25 The system simulink simulation

Niu *et al. Robotics and Biomimetics* (2015) 2:2

Page 13 of 14
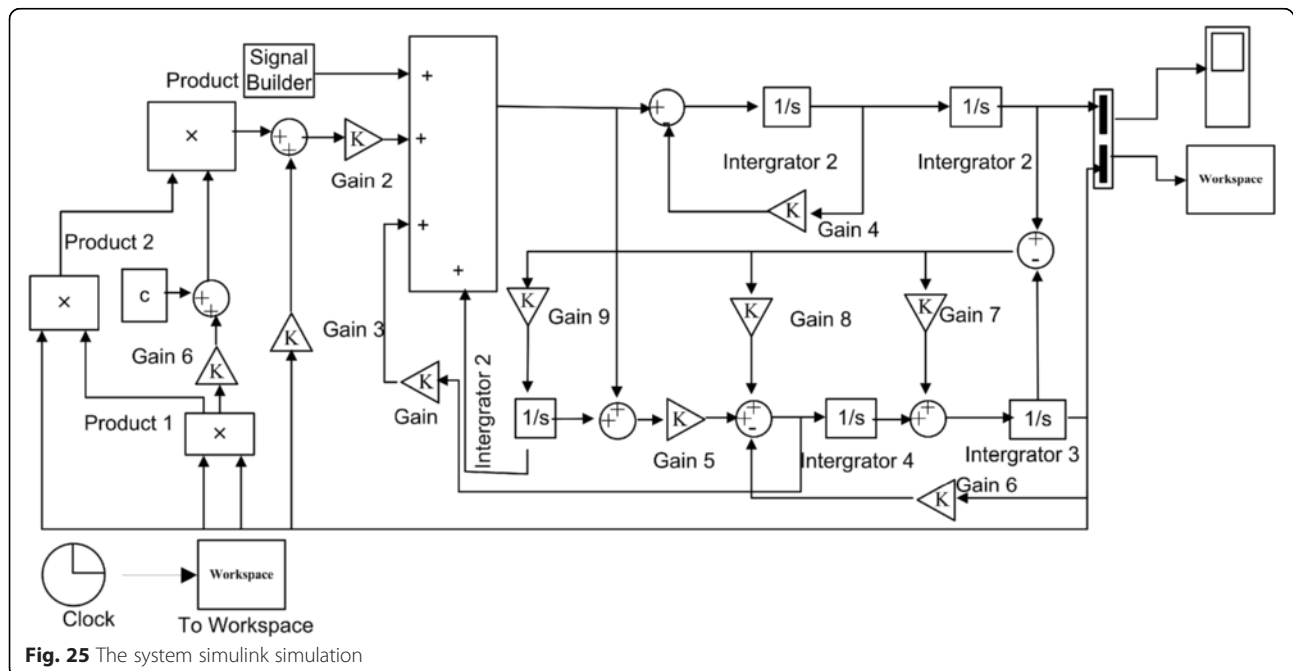
Fig. 26 The joint position changes in tinny disturbance under different pole configuration. (**a**) Three times, (**b**) six times, (**c**) eight times, and (**d**) nine times

environment spend 95 % of the time in a 60° cone with a tip located at the port. In addition, in order to reach the full extent of the abdomen, the tool needed to be moved 90° in the lateral/medial direction (left to right) and 60° in the superior/inferior (foot to head) direction. The workspace of the triangle mechanism is shown in Fig. 24, and the workspace is 102° cone; the tool can be moved 180° in the left to right and 102° in the foot to right. The workspace meets the requirement.

In order to validate resistance compensation, resistance compensation block diagram is shown in Fig. 25. A small perturbation excitation is added to the system. The system will produce large motion which is shown in Fig. 26. The simulation result validates the resistance compensation method.

Conclusions

A new RCM mechanism called the triangle mechanism is proposed. The mechanism performance analysis of the triangle mechanism and optimization of the triangle mechanism are achieved, the best α_1 and α_2 is 74° and 51°, respectively. Then, the RCM mechanism is built up. A new preoperative adjustment method achieved by resistance compensation method is proposed, and the dynamic equation of triangle mechanism is deduced. The simulation results validate the resistance compensation method.

References
1. Hagn U, Konietschke R, Tobergte A, Nickl M, Jörg S, Kübler B, Passig G, Gröger M, Fröhlich F, Seibold U, Le-Tien L, Albu-Schäffer A, Nothhelfer A, Hacker F, Grebenstein M, Hirzinger G (2009) DLR MiroSurge: a versatile system for research in endoscopic telesurgery. Int J Comput Ass Rad 5(2):183–193
2. Hagn U, Nickl M, Jörg S, Bahls T, Nothhelfer A, Hacker F, Le-Tien L, Albu-Schaffer A, Konietschke R, Grebenstein M, Warpup R, Haslinger R, Frommberger M, Hirzinger G (2008) The DLR MIRO: a versatile lightweight robot for surgical applications. Ind Robot 35(4):324–336
3. Stark M, Benhidjeb T, Gidaro S, Morales RE (2012) The future of telesurgery: a universal system with haptic sensation. J Turk Ger Gynecol Assoc 13(1):74–76
4. Madhani A J, Niemeyer G, Salisbury Jr J K (1998) The Black Falcon: a teleoperated surgical instrument for minimally invasive surgery. In: Intelligent Robots and Systems (IROS), 1998 IEEE/RSJ International Conference on, IEEE, Victoria, BC, Canada, pp936-944
5. Taylor RH, Funda J, Eldridge B, Gomory S, Gruben K, LaRose D, Talanmin M, Kavoussi L, Anderson J (1995) A telerobotic assistant for laparoscopic surgery. IEEE Eng Med 14(3):279–288
6. Nawrat Z, Podsedkowski L, Mianowski K, Wroblewski P, Kostka P, Baczynski M, Malota z, Granosik G, Jexierski E, Wroblewska A, Religa Z (2002) Robln Heart in

Niu *et al. Robotics and Biomimetics* (2015) 2:2

Page 14 of 14

2002—actual state of Polish cardio-robot. In: Robot Motion and Control (RoMoCo), 2002 Proceedings of the Third International Workshop on, IEEE, Bukowy Dworek, Poland, pp33-38

7. Nawrat Z, Kostka P (2006) Polish cardio-robot 'Robin Heart' System description and technical evaluation. Int J Med Robot Comp 2(1):36–44

8. Guthart G, Salisbury Jr J K (2000) The Intuitive TM telesurgery system: overview and application. In: Robotics and Automation (ICRA) 2000 IEEE International Conference on, IEEE, San Francisco, CA, USA, pp 618–621

9. Cavusoglu MC, Williams W, Tendick F, Sastry SS (2003) Robotics for telesurgery: second generation Berkeley/UCSF laparoscopic telesurgical workstation and looking towards the future applications. Ind Robot 30(1):22–29

10. Kim J, Lee Y, Ko S, Kwon D, Lee W (2004) Compact camera assistant robot for minimally invasive surgery: KaLAR. In: Intelligent Robots and Systems (IROS), 2004 IEEE/RSJ International Conference on, IEEE, Sendai, Japan, pp 2587–2592

11. Kang H, Wen J T (2001) Endobot: a robotic assistant in minimally invasive surgeries. In: Robotics and Automation (ICRA) 2000 IEEE International Conference on, IEEE, Seoul, Korea, pp 2031–2036

12. Kang H (2002) Robotic assisted suturing in minimally invasive surgery. Dissertation, Rensselaer Polytechnic Institute

13. Berkelman P, Cinquin P, Troccaz J, Ayoubi J, Letoublon C, Bouchard F (2002) A compact, compliant laparoscopic endoscope manipulator. In: Robotics and Automation (ICRA) 2000 IEEE International Conference on, IEEE, Washington. DC, USA, pp1870-1875

14. Lum MJ, Friedman DC, Sankaranarayanan G, King H, Fodero K, Leuschke R, Hannaford B, Rosen J, Sinanan MN (2009) The raven: design and validation of a telesurgery system. Int J Robot Res 28(9):1183–1197

15. Zemiti N, Morel G, Ortmaier T, Bonnet N (2007) Mechatronic design of a new robot for force control in minimally invasive surgery. IEEE ASME Trans Mechatron 12(2):143–153

16. Kim S, Shin W, Ko S, Kim J, Kwon D (2008) Design of a compact 5-DOF surgical robot of a spherical mechanism: CURES. In: Advanced Intelligent Mechatronics (AIM) 2008 IEEE/ASME International Conference on, IEEE, Xi'an, China, pp 990–995

17. Saing V, Sotthivirat S, Vilasrussamee R N, Suthakorn J (2008) Design of a new laparoscopic-holder assisting robot. In: Biomedical Engineering (ISBME), 2008, the 3rd International Symposium on, American Scientific Publishers, Grand Mercure Fortune Bangkok, Thailand, pp 278–281

18. Hsu J K, Li T, Payandeh S (2005) On integration of a novel minimally invasive surgery robotic system. In: Robotics and Automation (ICRA) 2005 IEEE International Conference on, IEEE, Seattle, WA, USA, pp 437–444

19. Sackier JM, Wang Y (1994) Robotically assisted laparoscopic surgery. Surg Endosc 8(1):63–66

20. Ghodoussi M, Butner S E, Wang Y (2002) Robotic surgery—the transatlantic case. In: Robotics and Automation (ICRA) 2002 IEEE International Conference on, IEEE, Washington, DC, USA, pp 1882–1888

21. Funda J, Gruben K, Eldridge B, Gomory S, Taylor R (1995) Control and evaluation of a 7-axis surgical robot for laparoscopy. In: Robotics and Automation (ICRA) 1995 IEEE International Conference on, IEEE, Nagoya, Jpn, pp 1477–1484

22. Gossenlin C, Angeles J (1991) A global performance index for the kinematic optimization of robotic manipulators. J Mech Design 113(3):220–226

23. Shi Z-X, Luo Y-F, Chen H, Ye M-Y (2005) On global performance indices of robotic mechanisms. Robot 27(5):420–422

24. Guo X J (2010) Theory and simulation of mechanism performance index, Science Press. Beijing, China

25. Stephens D W (1986) Foraging theory, New Jersey, Princeton University Press. USA

26. Lum MJ, Rosen J, Sinanan MN, Hannaford B (2004) Kinematic optimization of a spherical mechanism for a minimally invasive surgical robot. In: Robotics and Automation (ICRA), 2004 IEEE International Conference on, IEEE, New Orleans, LA, USA, pp 829–834